Materials Today Communications 34 (2023) 104977

Contents lists available at ScienceDirect

Materials Today Communications

journal homepage: www.elsevier.com/locate/mtcomm

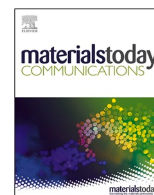

Inhibition of interlayer diffusion and reduction of impurities in thin metal films by ion irradiation

I.O. Kruhlov [a,*], A.K. Orlov [a], O. Dubikovskyi [a,e], Y. Iguchi [d], Z. Erdélyi [d], S.I. Sidorenko [a], T. Ishikawa [c], S.V. Prikhodko [b], S.M. Voloshko [a]

[a] National Technical University of Ukraine "Igor Sikorsky Kyiv Polytechnic Institute", Prospect Peremogy 37, 03056 Kyiv, Ukraine
[b] University of California Los Angeles, 2121K-Engineering 5 420 Westwood Plaza, CA 90095–1595, USA
[c] RIKEN SPring-8 Center, 1-1-1 Kouto, Sayo-cho, Sayo-gun, Hyogo 679–5148, Japan
[d] University of Debrecen, POBox 400, H-4002 Debrecen, Hungary
[e] V.Ye. Lashkaryov Institute of Semiconductor Physics (ISP), Prospect Nauki 41, 03028 Kyiv, Ukraine

ARTICLE INFO

Keywords:
Thin films
Diffusion
Low-energy ion irradiation
Impurities
Annealing

ABSTRACT

The effect of pre-irradiation on a stack of metal multilayer thin films (MLTF) with low-energy Ar^+ ions followed by thermal annealing of the stack has been studied. A three-layer Ni/Cu/V structure represented the as-fabricated MLTF samples. Each layer had a thickness of 25 nm. The entire assembly was built on Si using magnetron sputtering with different targets. The samples were pre-irradiated with Ar^+ ions at 400 and 800 eV. After the irradiation, the samples were further annealed at 450 °C for 15 min in an argon atmosphere. The structure, phase, and chemical composition of the MLTF samples were examined using X-ray diffraction, Auger electron spectroscopy, and secondary ion mass spectrometry. The distribution of the primary and impurity elements in the MLTF stacks was studied before and after the treatment, determining the diffusion ability of each element and changes they cause. It was found that applying the irradiation before annealing inhibited the diffusion of Ni and V atoms into the Cu layer. In addition, samples after pre-irradiation demonstrated lower oxygen and carbon impurities in the Cu layer. The degree of oxidation in the Ni and Cu layers was also reduced. The most notable cleaning effect of the Cu layer occurred for the sample that was pre-irradiated at 800 eV.

1. Introduction

Due to their high electrical and thermal conductivity and good electromigration resistance, Cu-based nanoscale thin films are among the most promising materials used in micro and nanoelectronics [1]. They are also considered an alternative for silver paste contacts in the photovoltaic industry [2–4]. Replacing noble metals with Cu in electronic contacts without compromising functionality would significantly reduce the cost of making solar panels. Since silver contacts account for up to 30% of the cost of manufacturing solar cells today [5], replacing the Ag with Cu would generate substantial cost savings since the unit cost of Cu is about 80 times cheaper than Ag [2].

However, such prospects are not flawless. The biggest challenge with replacing Ag with Cu is due to the higher diffusion activity of the latter. Diffusion-related obstacles may be evidenced in the formation of intermetallics that serve as recombination centers [6], the porous structure of the Cu/Si interface [7], and the relatively poor adhesion of Cu to Si substrates [8]. Another problem is low oxidation resistance of Cu, even under vacuum conditions [9]. Ultimately, these problems must be resolved to make Cu a feasible replacement for Ag in solar cell contacts. One solution for the low Cu oxidation resistance is to add a capping layer of other metals with higher oxidation resistance, for example, Ni or Au [1,10]. To overcome the challenges of unsatisfactory adhesion and peeling of the Cu contact, an additional metal buffer layer can be used, such as Ti, Ru, Cr, V, or Ta [11–14]. With this addition, a diffusion interaction between the buffer layer and Cu can occur at elevated temperatures, impairing the contact's electrical conductivity. Cu atoms can diffuse and spread along grain boundaries and dislocation networks with agglomeration on the outer surface of the film, even at relatively moderate temperatures around 200 °C [7], which can cause the formation of micro- and nanopores with a corresponding increase in contact resistance and disruption of the interfaces' integrity. Propagation of structural defects through the bulk of multi-films assembly may also happen due to the Kirkendall effect, when the buffer layer material diffuses to

* Corresponding author.
E-mail address: ivankruhlov@gmail.com (I.O. Kruhlov).

https://doi.org/10.1016/j.mtcomm.2022.104977
Received 27 June 2022; Received in revised form 30 October 2022; Accepted 19 November 2022
Available online 21 November 2022
2352-4928/© 2022 The Author(s). Published by Elsevier Ltd. This is an open access article under the CC BY-NC-ND license (http://creativecommons.org/licenses/by-nc-nd/4.0/).

the outer surface into the cupping layer film and is oxidized. For instance, that could happen if Cr were used for the buffer layer, but it would not happen for V [15].

An equally important limitation with the long-term stability of metal contacts is their possible saturation with light impurities (C, O, etc.), which, depending on the severity of this process, can impair the device's functionality. Contaminants may be introduced into the film during its fabrication or through subsequent exposure to the environment [9]. The atmosphere inside the deposition chamber may be a likely source of contaminants for the growing films, particularly when the low deposition rate of the elements and low deposition pressure within the chamber are applicable, inhibiting the fabrication of pure metal films [16]. An almost identical result of substantial impurities saturation of the thin layer of Cr film with C (24–26 at%) and O (30–31 at%) was reported, regardless of the deposition technique used: electron beam deposition or rf magnetron sputtering [17]. The structure exposure to the environment during device operations can also introduce contamination and oxidation to the film. Native oxidation of Cu thin films occurs when they are exposed to ambient air. It was found that a Cu_2O layer forms immediately after such exposure, and the thickness of the layer grows to 2.5 nm ($\pm$ 0.2 nm) after 1 h [18]. The thickness of the oxide layer reached 4 nm ($\pm$ 0.4 nm) after 5 days of air exposure, and its subsequent growth was less pronounced. These contamination-related problems must be resolved for the nanoscale functional materials due to their unpredictable effect on the long-term operational properties of the structures.

As shown recently, irradiating a Ni(25 nm)/Cu(25 nm)/Cr(25 nm) thin-film assembly with low-energy Ar^+ ions has a positive effect on the oxidation resistance and chemical purity of the Cu conductive layer [19]. Optimal irradiation conditions were determined in the highest values of the metal layers' passivation coefficients, and a significant decrease of O and C content remained in the film after magnetron sputtering. Since no heat treatment was used in this study, no diffusion processes were detected.

Elevated temperatures are inevitable during the operation of actual solar cell devices. Therefore, the multilayer thin-film (MLTF) metal assemblies, serving as their electrical contacts, must be resistant to diffusion processes that are both internal (intermixing of the film's components) and external (adsorbing elements from the ambient environment). This becomes one of the critical factors determining the entire system's functional properties and long-term stability. In addition, changes in the composition of the annealing atmosphere can substantially affect diffusion behavior. It has been recently reported [20] that the thermal stability of MLTF of Ni(25 nm)/Cu(25 nm)/V(25 nm) is higher in a vacuum compared to an Ar atmosphere due to the faster diffusion of the films' components in the latter case.

It is important to avoid introducing impurities into thin-film metal structures from the surrounding atmosphere both during the deposition step and later during operation because of the unpredictable effect on the long-term functional stability of the elements. Therefore, a motivation for the present work was to study the feasibility of stabilizing the multilayer thin-film metal structure and its resistance to likely diffusion processes by irradiating the structure with low-energy Ar^+ ions prior to thermal treatment of the structure in the Ar atmosphere. The study was performed on a Ni(25 nm)/Cu(25 nm)/V(25 nm) thin-film assembly deposited on the Si substrate using DC magnetron sputtering. The layers for this assembly included Ni for capping, Cu for conducting, and V for the buffer layer.

2. Material and methods

The MLTF assembly Ni(25 nm)/Cu(25 nm)/V(25 nm), the cap/conductor/buffer layer, respectively, was fabricated by a DC magnetron sputtering using high-purity Ni (99.995), Cu (99.99), and V (99.95, all at %) targets. The deposition was made on Si (100) single-crystal substrates at room temperature. Sputtering rates of 0.5 nm/s, 0.27 nm/s, and 0.065 nm/s were set for Cu, Ni, and V, respectively. The pre-sputtering chamber pressure was 2.0×10^{-5} Pa, while the argon pressure was maintained at 6.0×10^{-1} Pa during the sputtering. The thicknesses of the film layers were calculated from the known sputtering rates of the corresponding targets and further verified by depth profiling. The chosen thickness should satisfy both experimental and application requirements for advanced thin-film or flexible solar cells. From an experimental viewpoint, the thickness of the layers should be small enough so that depth profiling can be carried out using SIMS and AES techniques in a reasonable time. At the same time, it should also be large enough for reliable XRD measurements. The Si substrate was ultrasonically cleaned before deposition without removing the native oxide SiO_2 layer. The silicon wafer with deposited films was cleaved into 8 pieces, then subjected to different treatments. The sample processing conditions are summarized in Table 1. The annealing of samples was carried out under argon pressure at 200 Pa within the temperature range of 300–550 °C for 15 min at a heating rate of 2 °C/s. Before annealing the background vacuum in chamber was pumped up to 10^{-4} Pa.

The effect of additional ion pre-irradiation on the diffusion behavior of the elements upon annealing was explored at a temperature of 450 °C (see the Experimental section for details). Two samples (Table 1, samples 4–2 and 4–3) were subjected to low-energy (400 eV and 800 eV) ion irradiation prior to 450 °C annealing. In the following, this type of two-step processing consisting of ion pre-irradiation followed by annealing will be referred to as the complex treatment. Ion pre-irradiation was carried out using Ar^+ ions at the Omegatron OMI-0010 source with a fluence of 5.6×10^{16} ion/cm^2 at normal beam incidence. The choice of ion energies and fluence was based on the previously reported optimal modes of Ar^+ irradiation providing the effect of impurities release [19]. The fluence was preliminarily calibrated using a standard Faraday cup. Since low beam energies were applied, no noticeable heating of the samples was observed upon irradiation, controlled by a *K*-type thermocouple mounted at the film surface. After sputtering, the residual thickness of the Ni upper layer was evaluated to check the partial removal of material during the ion irradiation by surface profilometry using a SurfCorder ET 4000 LS device with a load of 10 μN. The residual thickness of the Ni film was 20.5 nm ($\pm$ 1 nm) and 16.8 nm ($\pm$ 1 nm) for samples irradiated with beam energies of 400 eV and 800 eV, respectively. Finally, an experimental study of all samples was conducted ex-situ using structural and chemical analytical techniques.

X-ray diffraction (XRD) analysis of the samples was performed using a θ-2θ scanning mode with Cu-Kα radiation (1.5405 Å) on a Rigaku ULTIMA IV diffractometer. AES depth profiling was performed on a Jamp-9500F (Jeol) system by etching the film with 1 keV Ar^+ ions at a 45° angle to the sample surface. The spectra were recorded using a primary electron beam of 10 keV energy and a current of 30 nA. Auger electron elemental mapping was taken along the etching crater at a sample inclination angle of 30°. Secondary ion mass spectrometry (SIMS) was performed using an Ion Time-of-Flight IV device with a primary beam of 1 keV positive O^+ ions and 2 keV negative Cs^- ions. 3D visualization of the secondary ions' distribution was realized from a 1×1 μm^2 area in the center of the ion etching crater to prevent the crater wall effect. The complex application of primary O^+ and Cs^- ions

Table 1
The parameters for the sample treatment.

Sample no.		(Ion irradiation)	➡ Annealing
1		*no irradiation*	as-dep.
2		*no irradiation*	300 °C, 15 min
3		*no irradiation*	400 °C, 15 min
4		*no irradiation*	450 °C, 15 min
	4–1	400 eV	450 °C, 15 min
	4–2	800 eV	450 °C, 15 min
5		*no irradiation*	500 °C, 15 min
6		*no irradiation*	550 °C, 15 min

allowed us to get complete information on the film's chemical composition to track the distribution of O and C impurities and fragmentary NiV, CuNi, and CuV ions.

3. Results

As noted above, functional metal thin-film assemblies exposed to elevated temperatures had to be resistant to both diffusion between metal film layers and permeation of light element impurities into the structure from the environment. The experimental results chapter is divided into two corresponding sections to address these effects separately, while their interrelation and interpretation are reviewed in the Discussion section.

3.1. Interlayer diffusion

All XRD spectra were taken in the *2θ* diffraction range of 10–70 degrees; however, the two most prominent Cu and Ni peaks, namely {111} diffraction, could be seen in the range of 42–47°, as shown in Fig. 1. The as-deposited sample demonstrated two well-separated peaks {111} of the face-centered cubic (fcc) Ni at 44.613° and fcc Cu at 43.373°. The absence of V diffraction in the entire measured range suggests it formed an amorphous or ultrafine-grained structure during the deposition. That is not a particularly new finding [20] and is most likely related to V deposition on the cold substrate at the relatively low sputtering rate, which was 0.065 nm/s. As the annealing temperature increased to 300 °C, the position of the Cu (111) peak shifted towards higher angles, indicating the onset of diffusion reactions between layers. Further increases in the annealing temperature resulted in further shifting of this Cu peak. Moreover, starting at 400 °C, the shift of the Ni peak towards Cu was also detected, while at 550 °C, these two peaks merged into one at 43.878°, corresponding to {111} peak of the Cu-Ni solid solution. It is worth noting that according to the Ni-Cu binary phase diagram, they have unlimited solubility in each other, tending to form a substitutional solid solution at elevated temperatures.

The corresponding change in lattice parameter of the samples is shown in Fig. 2, where (a) shows a change in the lattice as a function of the annealing temperature and (b) as a function of complex treatment with various ion energy a constant annealing temperature of 450 °C. The lattice constants of Cu and Ni of the as-deposited MLTF stack were 0.3608 nm and 0.3515 nm, respectively. The onset of the diffusion-driven formation of a Cu-based substitutional solid solution was detected after annealing at 300 °C, accompanied by a decrease in the Cu lattice parameter to 0.3600 nm. Based on Vegard's law approximation [21], the composition of the solid solution corresponded to $Cu_{92}Ni_{08}$. Annealing at 400 °C was accompanied by a further decrease in the Cu lattice parameter, associated with increased content of Ni substitutional atoms in the Cu-based solution, making its atomic composition $Cu_{74}Ni_{26}$. Similarly, when the annealing temperature increased to 500 °C, the atomic fraction of Ni solutes in Cu rose, making $Cu_{67}Ni_{33}$ with a lattice parameter measured at 0.3578 nm. The subsequent increase of the annealing temperature to 550 °C led to the formation of an almost equiatomic $Cu_{53}Ni_{47}$ solid solution with a lattice parameter measured at 0.3568 nm.

The lattice constant of Ni changed at 400 °C, indicating the formation of a second solid solution, with Ni as a matrix and Cu as a solute. The atomic composition of this Ni-based solution changed to $Ni_{80}Cu_{20}$ after 500 °C annealing. It is worth noting that the formation of a Ni-based

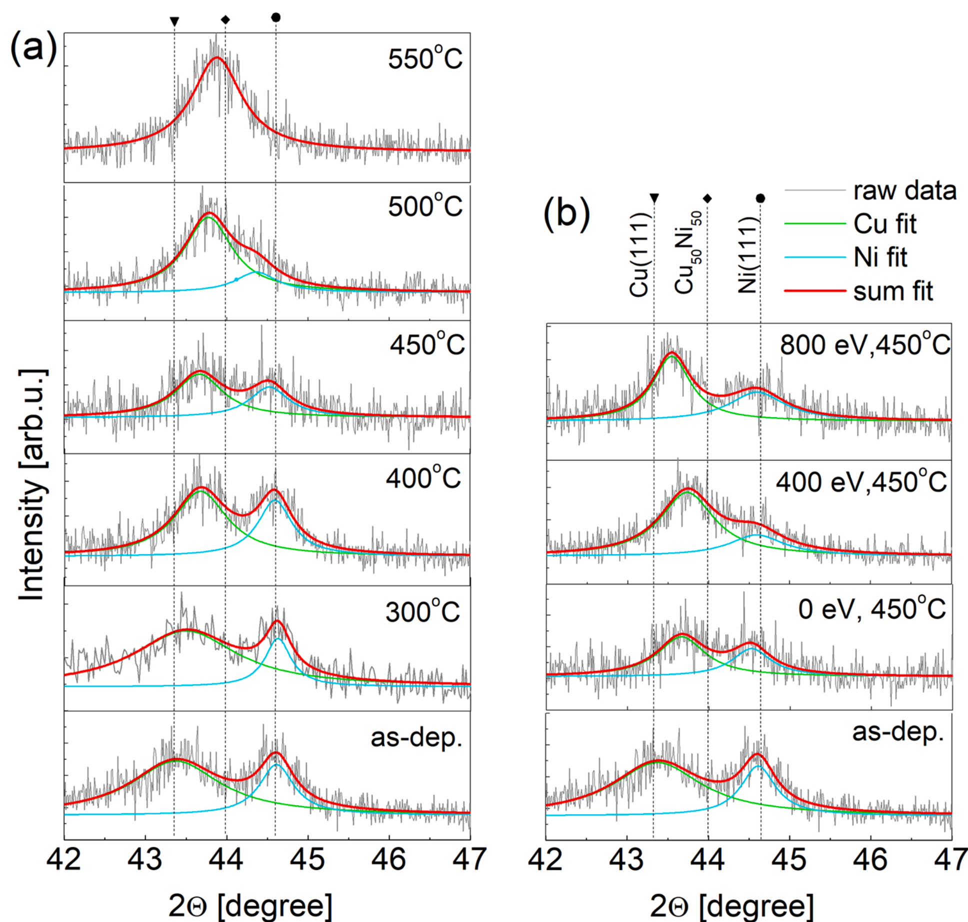

Fig. 1. XRD scans of thin-film samples as-deposited and (a) after additional annealing in the temperature range of 300–550 °C; (b) after 450 °C annealing following ion irradiation with different energy.

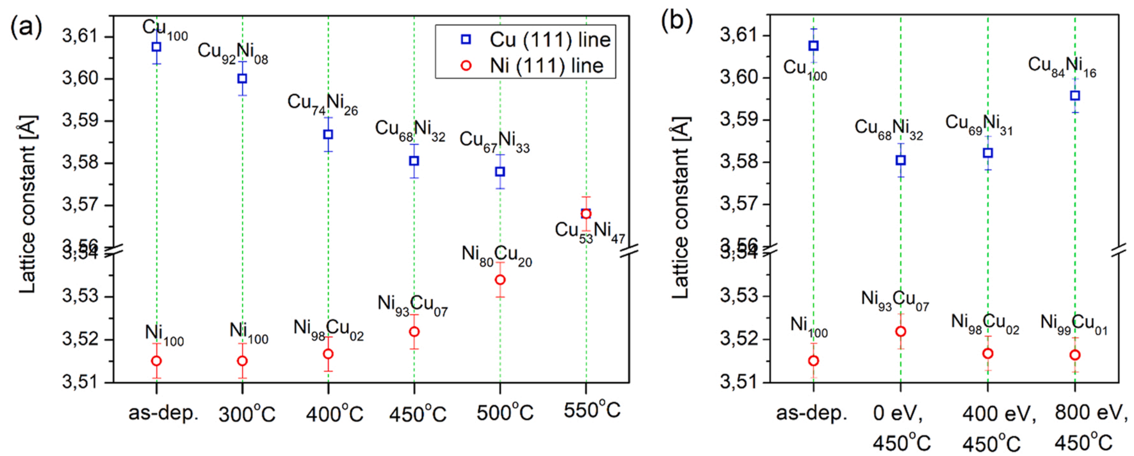

Fig. 2. Lattice constants of Cu and Ni films as-deposited and (a) after annealing in the temperature range of 300–550 °C and (b) after complex treatment with different energy. The atomic composition of the formed solid solutions was estimated based on the XRD data using Vegard's law approximation.

solution started at a higher annealing temperature than the Cu-based one. For instance, the Cu-based $Cu_{92}Ni_{08}$ solid solution formed after 300 °C annealing, while the Ni-based $Ni_{93}Cu_{07}$ solution of a similar atomic ratio was observed at a higher temperature of 450 °C, a difference of about 150 °C. The difference in the kinetics of these solid solutions formation can be attributed to the lower diffusivity of Cu in Ni compared to the Ni in Cu diffusivity [22].

The presented XRD data indicates that the widespread diffusion interplay between Ni and Cu already occurred at 450 °C in each layer; however, it did not result in a complete intermixing of the components with homogenization of the elemental composition through the film depth. This temperature was used for the complex treatment of samples to investigate the effect of pre-irradiation on the diffusion behavior upon the next annealing. Related samples are listed in Table 1 as 4–1, 4–2, 4–3; all were annealed at 450 °C after no irradiation (labeled as 0 eV) and irradiation with 400 eV and 800 eV, respectively.

The layer-by-layer elemental composition measurement of the samples after deposition and different treatments was done using AES depth profiling data, shown in Fig. 3. The as-deposited sample (Fig. 3, a) had clear interfaces between all layers, indicating no diffusion interplay between the components, while some overlapping of signals could be attributed to the limited in-depth resolution of the AES. The observed difference in the width of Ni, Cu, and V profiles was related only to their different sputtering yield rates (Cu = 320 Å/s, Ni = 190 Å/s, V = 85 Å/

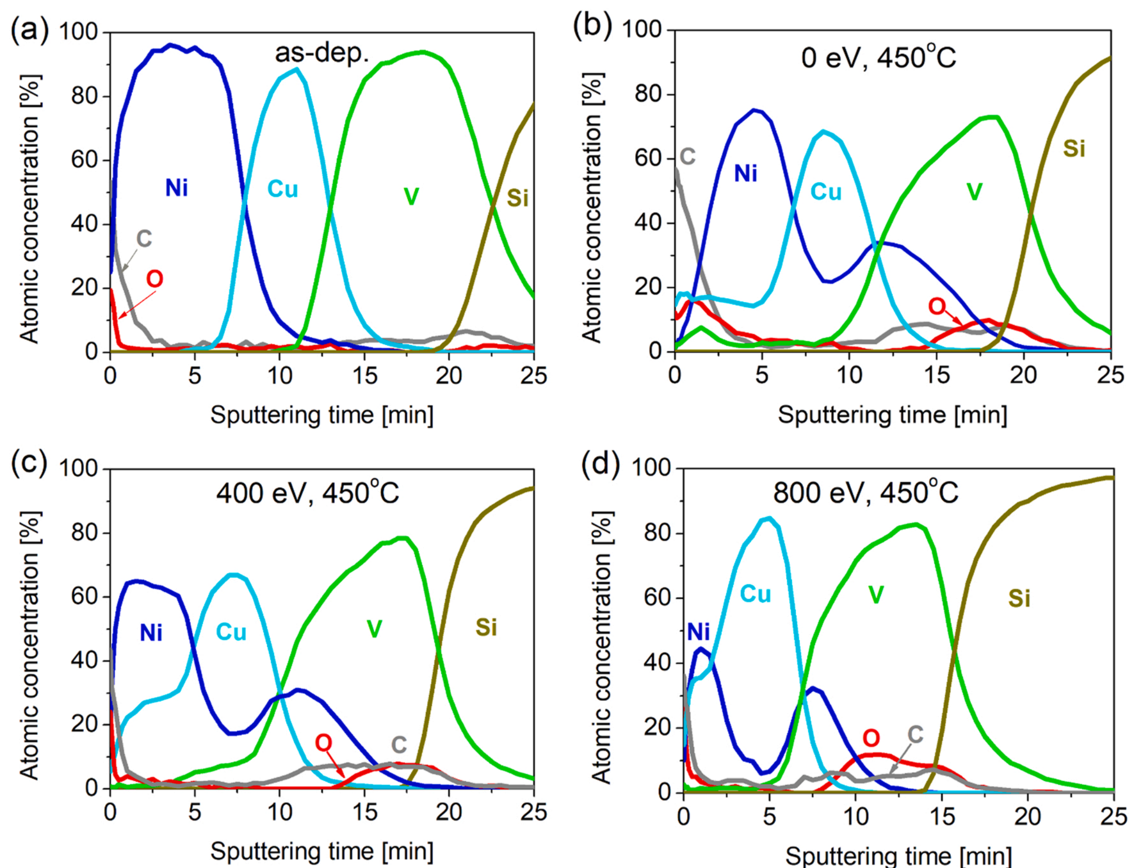

Fig. 3. AES depth profiling results of the thin films after deposition (a), annealing at 450 °C (b), and complex treatment with 400 eV (c) and 800 eV (d) ions.

s) but not to the alteration of actual thicknesses of the metal films.

Annealing at 450 °C (Fig. 3, b) resulted in Cu diffusion towards the outer surface and the concentration of Cu in Ni reached 15–20 % (hereinafter in at%). Ni also diffused through the Cu layer, making an uneven distribution. Inside the Cu layer, the Ni content was about 20 %, while near the Cu/V interface, it had a splash of about 30 %. A moderate diffusion of V to the outer surface was also detected after annealing. The V concentration at the surface reached up to 10 % and its oxidation was likely due to its high affinity to oxygen.

Both the XRD and AES data confirm the metals were intermixing; however, the substantially different atomic content of Cu solute in the Ni layer was detected by these two techniques, namely ~7 % as measured by XRD (Fig. 2) and ~18 % by AES (Fig. 3). Most likely, this discrepancy related to the multi-stage diffusion, which is a classical behavior for solid solutions with unlimited solubility of components. The Vegard law was applied to estimate the atomic composition of the formed solid solution based on XRD data, which characterized the structural changes in the material's crystal lattice. On the other hand, Auger profiling data showed the average in-depth elemental distribution, regardless of the chemical elements were associated with the bulk (particular crystal lattice) or grain boundary. Thus, the observed discrepancy in Cu content measurements may have resulted from these atoms occupying substitutional sites in the Ni lattice and segregating at grain boundaries. As a result, the Auger profiling detected more than two times higher concentration of Cu in the Ni layer. At the same time, the Ni concentration in Cu estimated with both Vegard's approximation and AES data was close, indicating that diffused Ni was almost completely dissolved in the Cu matrix but not in its grains' boundaries. That is due to the difference between the diffusivities of Ni in Cu and Cu in Ni. The above observations suggest that the combination of the lattice and grain boundary mechanisms governs the interdiffusion between the Ni and Cu layers.

The intermixing of layers after annealing was also evident in the Auger electron elemental distribution maps shown in Fig. 4. Annealing the sample at 450 °C (Fig. 4, b) significantly blurred the layers' interfaces compared to the as-deposited state (Fig. 4, a).

Notable differences were seen in the diffusion behavior between the samples after annealing and complex treatment. The decrease of the Ni content in the Cu layer measured by Auger was particularly significant. It changed from 22 % at 0 eV to 17 % at 400 eV and to 6 % at 800 eV treated samples (Fig. 3, b-d). That change indicates a slowdown of the Ni diffusion into the Cu layer after the preliminary ion treatment was applied to the films' stack and this inhibition was stronger for the higher energy ion treatment used. As a consequence, the Cu-based film obtained fewer solutes. That complied with the XRD data, as the lattice constant of the Cu phase tended to its initial values (Fig. 2). The effect was more pronounced for the Cu-based solid solution as its formation ran faster due to higher atomic mobility of Ni in Cu. According to the components' concentration calculation using Vegard's law, the Ni content in the Cu-based solid solution decreased from 33 % for the annealed sample to 31 % after complex treatment with 400 eV and down to 16 % for the case of 800 eV.

It is also worth noting that the depth profiles after complex treatment did not demonstrate V diffusion to the outer surface, unlike the case of annealing only. Overall, we saw inhibiting of the diffusion of all elements, except Cu, after complex treatment, and the 800 eV irradiation mode provided the highest purity for the Cu layer. The higher concentration of Cu in Ni (Fig. 3, c, d) registered for the samples after complex treatment is likely due to the instrumental artifact associated with the crater walls effect [23]. Notably, the thinner the Ni layer that remained after the ion irradiation stage, the more pronounced was the effect of the non-flat-bottom crater during SIMS profiling measurement.

The SIMS results using primary O_2^+ ions are shown in Fig. 5. This data complies with the XRD and AES results presented above. While the intensity of the Auger electron current mostly depended on the amount of the element used, the intensity of the secondary ion current, in addition to concentration, was also sensitive to the interatomic bonds [23], which revealed additional information. The distribution of fragmentary ions throughout the film's depth enabled the detection of solid solutions or chemical compounds at specific sites of the sample. This became possible as SIMS results showed the distribution of fragmentary NiV^+ and $NiCu^+$ ions in addition to primary ions.

The SIMS data suggests that diffusion of the main components was inhibited after additional ion irradiation (Fig. 5, c, d) compared to the annealed sample (Fig. 5, b). The signal of Ni in the Cu layer decreased significantly – the intensity of the Ni^+ signal in the Cu layer had an explicit minimum, which was most pronounced after the 800 eV complex treatment. It could also be determined from the SIMS data that the region of Ni and V diffusion interplay was reduced in the pre-irradiated annealed samples. The spread of fragmentary NiV^+ ions region was less for the complex treatment than for the annealing case. Furthermore, this area spread was smaller for the higher ion energy used, 800 eV. A similar result was observed for the distribution of fragmentary $NiCu^+$ ions. For the as-deposited film, only a weak signal from $NiCu^+$ arose at the Ni/Cu interface. After annealing, the diffusion-induced formation of Cu-Ni solid solutions was evidenced in a considerable broadening and increased intensity of the $NiCu^+$ signal. However, there was no gap seen between the regions of the two solutions. After complex treatment with 400 eV ions, the interaction region slightly decreased, showing a prominent minimum in $NiCu^+$ distribution. The treatment with 800 eV ions resulted in two distinguished regions of $NiCu^+$ distribution – the first was close to the outer surface while the second was at the Cu/V interface. Finally, a sharper drop of the NiV^+ peak on the Cu side indicated increased Cu chemical purity.

3.2. Diffusion of light impurities from the environment

The AES data (Fig. 3) shows the presence of some carbon and oxygen in Ni and V layers after deposition. Since no other impurities were measured at detectable concentrations, only these impurities were further studied in more detail. The presence of C in the surface area of thin films typically results from its adsorption from the atmosphere [24]. However, in the present case, C was also detected in the V bottom layer at an amount close to 5 %, even at room temperature (Fig. 3, a). It is worth noting that V has a high affinity to C, tending to the formation of

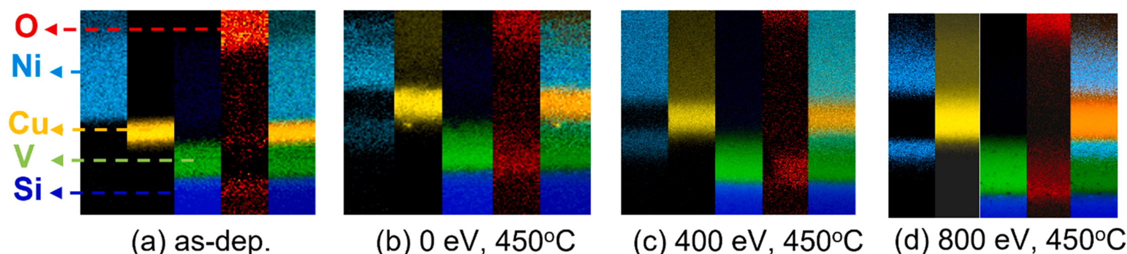

Fig. 4. Elemental maps with Auger electrons of the samples after deposition (a), annealing at 450 °C (b), and complex treatment with 400 eV (c) and 800 eV (d) ions. All maps were collected along the ion etching crater after depth profiling studies. The thickness of the layers shown in the map is not exact measure of the layer dimension, but rather reflection of the time of sputtering, which also depends on the type of sputtered atoms.

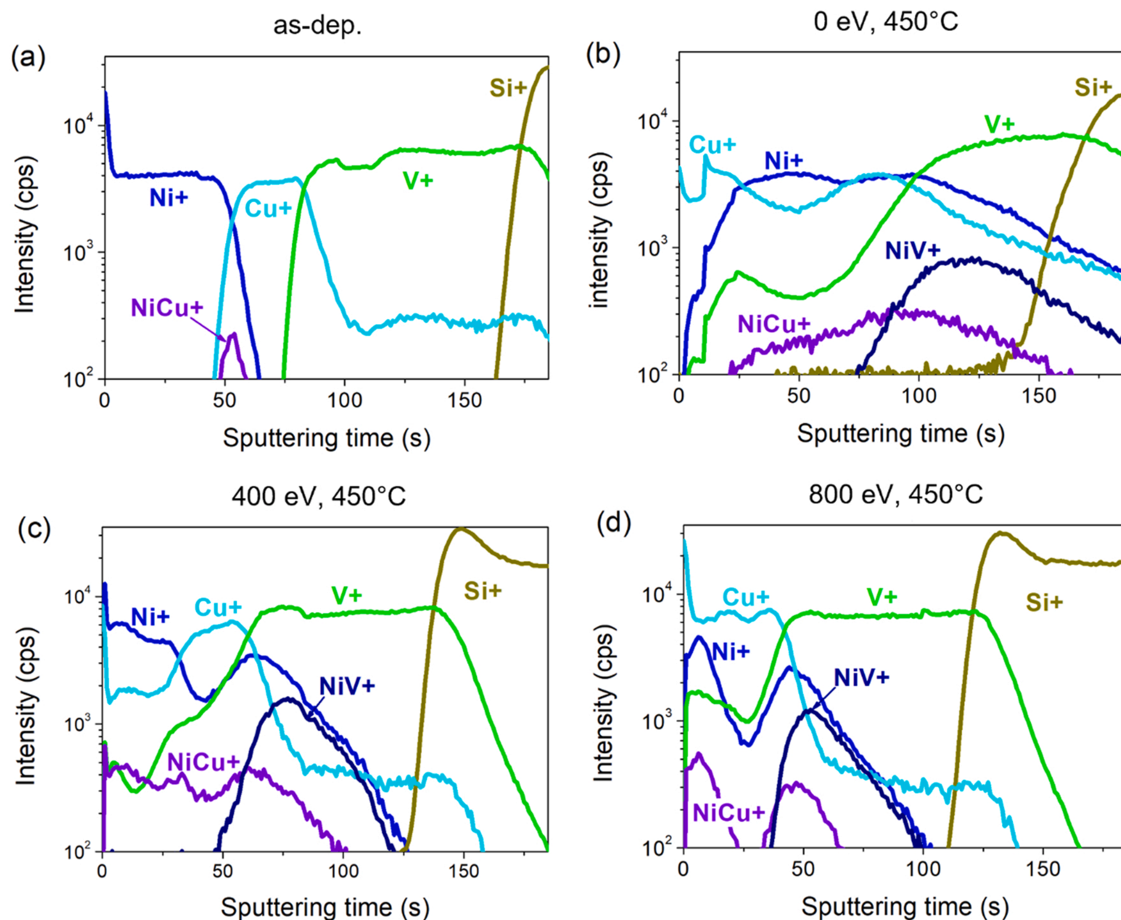

Fig. 5. SIMS depth distribution obtained using O^+ primary ions of the samples after deposition (a), annealing at 450 °C (b), complex treatment with 400 eV (c) and 800 eV (d) modes. To simplify data analysis, the intensity of V^+ secondary ion was reduced by 10^3.

carbides of various stoichiometry such as VC, V_8C_7, and V_6C_5 [25]. In addition to C, the Ni layer surface also showed the presence of O, as seen in the chemical mapping images taken along the film cross-section (Fig. 4, a). Some O was also detected at the V/Si and V/Cu interfaces, both due to the O adsorption from the atmosphere and the presence of SiO_2 native oxide. The high presence of contaminating impurities detected in V suggested the films were amorphous rather than ultrafine-grained, consistent with the earlier absence of V peaks on the XRD spectra.

The Auger depth profiling in Fig. 3 demonstrates that the annealing caused a significant increase in the C and O presence near the outer surface. Comparing the near-surface elemental composition for the films after annealing and complex treatments, it was concluded that the sputtering time (and thus the thickness) of the layer containing the O and C was roughly 3 times less for both of the complex modes. Furthermore, the depth propagation and the absolute value of the atomic content of impurities on the surface were substantially lower for the complex treatment than for simple annealing.

Fig. 6 shows the results of SIMS analysis using a primary beam of negative Cs^- ions, applied to increase sensitivity to carbon and oxygen as well as the oxygen-containing fragmentary ions due to the unparalleled elemental sensitivity (1 per 10^6 particles) of the technique [26]. The data presented in Fig. 6 agrees well with the observations obtained from the AES profiling discussed above.

In the as-deposited film (Fig. 6, a), the high intensity from O^- was registered on the outer surface and at the Cu/V and V/Si interfaces. After annealing (Fig. 6, b), the oxygen was evenly distributed over the depth of the film's stack. It is worth noting that both the AES and the SIMS data exhibited the increased presence of both C and O impurities after the annealing, signifying a saturation of the film by these light elements when exposed to elevated temperatures. However, ion pre-irradiation reduced the signal from O^- in the Cu layer and, most pronouncedly, in the region near the Cu/V interface. There was an explicit intensity minimum of O^- secondary ions at this site.

3D-distribution cubes of the secondary NiO^- oxide ions in Fig. 6, e demonstrate significant improvement of the Ni cap layer in resistance to oxidation for films after complex treatment compared to the annealed sample. While the intensity of NiO^- oxide increased dramatically for the sample after annealing, it remained moderate and localized in the near-surface region for the case of both modes of complex treatment.

A similar situation was observed for the secondary ions of CuO^- (Fig. 6, f). An increase in the CuO^- intensity was observed at the Ni/Cu and Cu/V interfaces in the initial state. After annealing, it was almost impossible to identify the Cu layer since oxidation occurred over the entire MLTF stack depth. However, after the complex treatment, the oxygen-free Cu layer could be well distinguished. CuO^- secondary ions were also detected at the Cu/V interface. The intensity of O^- after complex treatment decreased significantly compared to the annealing according to its signal distribution around this interface (Fig. 6, b-d).

Fig. 7 shows the SIMS data on C^- intensity in the Cu layer for all MLTF samples. It indicates that the intensity of carbon in Cu was reduced by 10 times for the 400 eV pre-irradiation and by 100 times for the 800 eV pre-irradiation compared to the regular annealing (0 eV).

Fig. 8 shows the aligned profiles of secondary Cu^+ ions in different samples. The maximum intensity of the Cu^+ signal after heat treatment was similar to the initial state, while it was 1.5 and 2 times higher after the 400 eV and 800 eV complex treatments. These results indicate the increased purity of the Cu film after complex treatment due to the lower

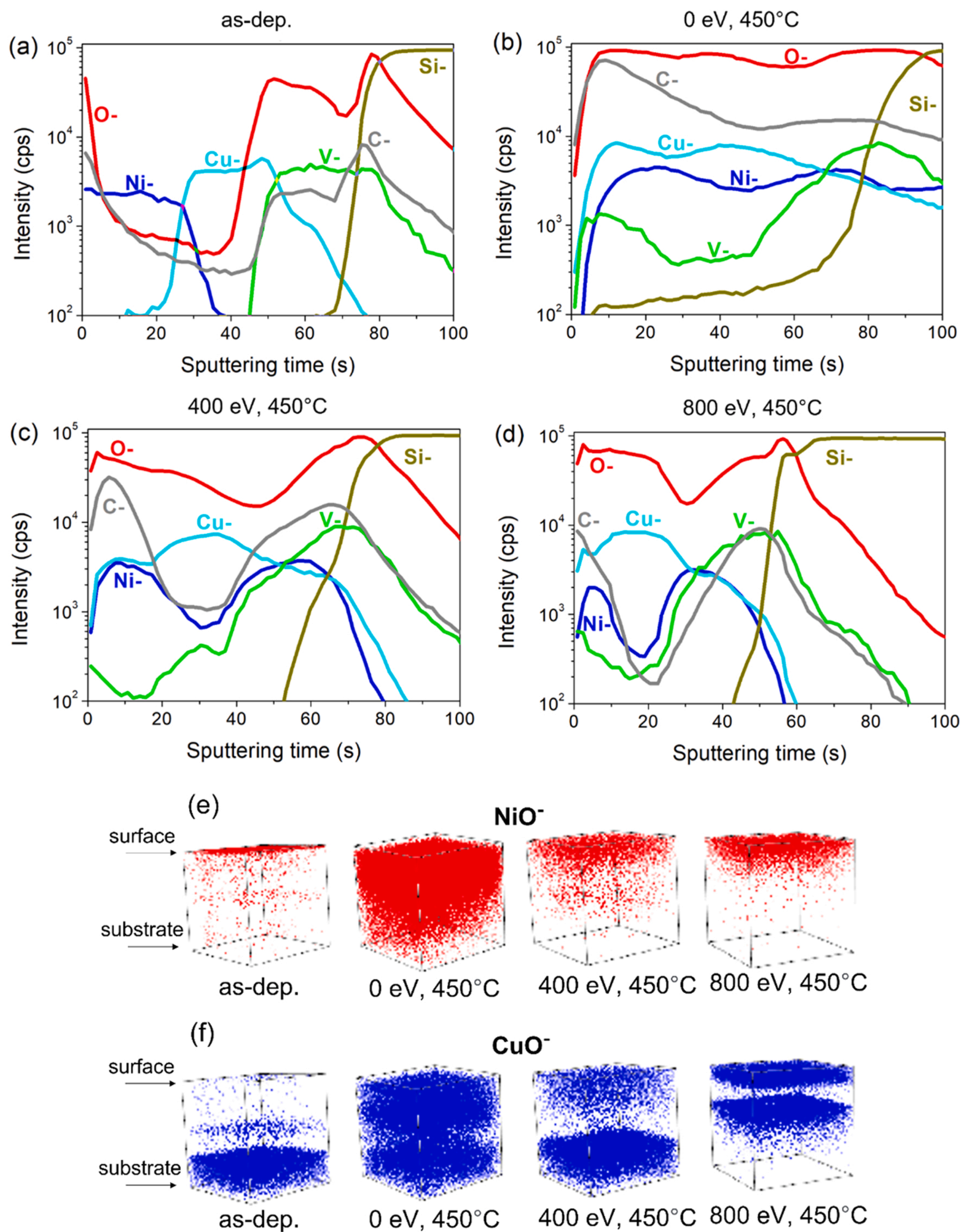

Fig. 6. SIMS depth distribution (obtained using Cs^- primary ions) of the secondary ions of principal components (Ni^-, Cu^-, V^-, Si^-) and impurities (O^-, C^-) of the samples after deposition (a), annealing at 450 °C (b), and complex treatment with 400 eV (c) and 800 eV (d) modes. 3D visualization of the distribution of NiO^- (e) and CuO^- (f) secondary ions oxides are shown as well.

content of impurities. They also agree well with the Auger electron mapping results in Fig. 4, d, which show an increase in the thickness and contrast of the Cu layer after 800 eV complex treatment. Most likely, impurities give the main components a higher noise signal so that a cleaning of the Cu film contributes to the corresponding increased contrast on the chemical map.

4. Discussion

The bulk of the presented experimental results suggests that the possible adverse effect of thermal annealing on the chemical stability of the main functional layer of Cu can be significantly improved by applying preliminary low-energy Ar^+ ion irradiation to the fabricated MLTF stack. The optimal regime for this ion irradiation is 800 eV energy. This treatment suppresses the diffusion of the main elements of the stack (Ni, V) into the conductive layer of Cu film and the diffusion of

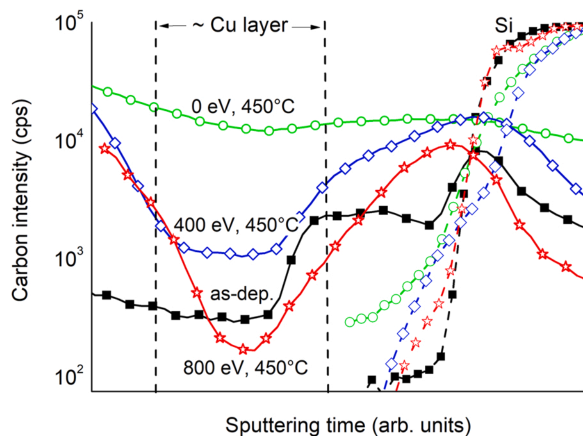

Fig. 7. Depth distribution of the C⁻ secondary ions intensity for the samples after deposition, annealing at 450 °C, and complex treatment with 400 eV and 800 eV modes based on SIMS profiling using Cs⁻ primary ions. For clarity, the profiles were aligned by the center of the Cu signal.

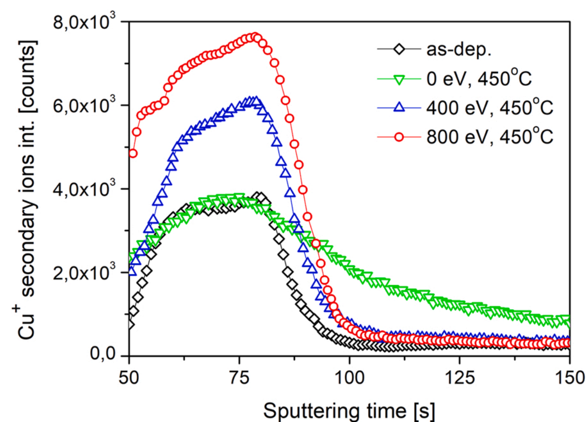

Fig. 8. The intensity of Cu^{+} secondary ions as a function of sputtering time during the SIMS depth profiling using O_2^{+} primary ions. To simplify data analysis, the profiles were aligned by the center of the Cu^{+} signal.

light impurities (C, O) during the subsequent annealing stage.

The substantial decrease in light interstitial impurities can be attributed to the low-energy ion irradiation stage. A similar effect has been reported elsewhere [19] for the Ni/Cu/Cr tri-layer stack when the low-energy Ar^{+} ion bombardment resulted in fewer light impurities (namely, carbon and oxygen) in the film. The present study utilized identically prepared systems employing the same technique and thicknesses of the same layers. The only difference was that V was used instead of Cr as a buffer layer. This replacement was made in the present study due to the higher thermal stability of V [15]. Therefore, an identical effect of impurities release compared to the non-treated system was most likely taking place in the present case for the samples irradiated with 400 eV and 800 eV ions. After the initial content of the impurities in the irradiated samples was changed, the positive effect remained after the next thermal treatment stage at 450 °C, most pronouncedly seen for 800 eV mode. In both cases the impurities release was found at the depth much exceeding the theoretical Ar^{+} projected ion range that is 0.8 nm for 400 eV and 1.1 nm for 800 eV according to the SRIM2010 calculations. However, this approach considers the ion range in perfect bulk Ni crystal, while the real ion range in thin-film Ni material could be substantially larger due to the higher number of structural defects, finer grains, larger contribution of surfaces and interfaces etc.

In addition to the decreased number of light impurities, a surprising result was discovered in the diffusion behavior of Ni and V in Cu. Their atomic mobility was noticeably suppressed for the samples when annealing followed the irradiation, again most pronouncedly for the 800 eV treatment, compared to the case of annealing only. Since ion irradiation causes some sputtering of the Ni layer, it is worth discussing whether there is a possible effect of Ni thickness on diffusion behavior and resulting elements redistribution. After irradiation, the remaining amount of Ni (17-nm-thick) is enough to overcome the whole Cu layer during annealing and agglomerate at the Cu/V interface with about 30 at% concentration. This concentration is similar after annealing for 0 eV (no irradiation), 400 eV and 800 eV modes, which indicates that the general diffusion behavior of Ni is not affected by its decreased thickness. Furthermore, the reduced thickness of Ni should predictably increase the content of V in Ni near-surface layer after complex treatment, as V diffusion path length towards the surface became smaller. However, this does not happen, vice versa the V content in Ni became smallest for 800 eV. The diffusion inhibition should be thus associated with the irradiation-induced release of the light interstitial impurities.

Depth profiling data indicate that diffusion inhibition is seen in the Cu layer, where the content of interstitial impurities is decreased. Numerous studies have reported strong binding between interstitial atoms of light impurities and vacancies in metals, leading to impurity-vacancy complexes [27–29]. For example, Kostler et al. reported [29] that the rise of carbon concentration in a Ni-C alloy from 0.25 at% to 0.78 at% resulted in an increased diffusivity of Co-60 tracer there from 3.77×10^{-11} cm^2/s to 5.55×10^{-11} cm^2/s, which was associated with the more significant number of vacancy-carbon defect pairs formed. So, the higher the carbon content, the more vacancies that are formed, therefore facilitating the solvent diffusion through the vacancy-mediated mechanism. It is likely that, in our case, the interstitial impurities also strongly bonded with vacancies, preventing their annihilation at the next annealing step. Therefore, fewer impurities remained in the Cu film after irradiation. The fewer impurity-vacancy stabilized pairs remained, and thus the smaller number of residual vacancies was present during annealing, correspondingly affecting the slowdown of Ni and V atomic mobility observed in the experiment.

5. Conclusions

The MLTF stack of Ni/Cu/V, each 25-nm-thick film, was successfully fabricated on a Si substrate using magnetron sputtering. It was shown that the thermal stability of the entire film stack, including the core functional Cu layer, could be significantly improved by applying preliminary low-energy Ar^{+} ion irradiation to the fabricated MLTF stack. It was found that the optimal regime of such ion irradiation was at 800 eV. The increase in stability of the structure during subsequent annealing was due to the observed inhibition of diffusion of the main elements of the film stack. Furthermore, it has been shown that after preliminary ion treatment, the number of light impurities, such as C and O, also decreased in the functional layer Cu at the subsequent annealing. The mechanisms of observed inhibition of diffusion of light impurities and the main elements of MLTF were discussed.

CRediT authorship contribution statement

I.O. Kruhlov: Formal analysis, Investigation, Visualization, Writing - original draft. **A.K. Orlov:** Formal analysis, Writing - review & editing. **O. Dubikovskyi:** Investigation. **Y. Iguchi:** Resources. **Z. Erdélyi:** Resources, Supervision. **S.I. Sidorenko:** Conceptualization, Project administration. **T. Ishikawa:** Funding acquisition, Project administration, Writing - review & editing. **S.V. Prikhodko:** Conceptualization, Supervision, Writing - review & editing. **S.M. Voloshko:** Conceptualization, Supervision, Writing - original draft; Writing - review & editing.

Declaration of Competing Interest

The authors declare that they have no known competing financial

interests or personal relationships that could have appeared to influence the work reported in this paper.

Data availability

No data was used for the research described in the article.

Acknowledgments

This publication is based on work supported by grant #G-202108–68019 from the U.S. Civilian Research & Development Foundation (CRDF Global). Any opinions, findings, conclusions, or recommendations expressed in this material are those of the authors and do not necessarily reflect the views of CRDF Global. This study was also partially supported by the Ministry of Education and Science of Ukraine, grants #0121U110283 and #0122U200166. The study was also supported by collaboration between the Igor Sikorsky Kyiv Polytechnic Institute, Ukraine, and the RIKEN SPring-8 Center, Japan, based on the Memorandum of Understanding from July 29, 2019. The research was also supported by the Thematic Excellence Program (TKP2020-IKA-04) of the Ministry for Innovation and Technology in Hungary.

References

[1] A. Bahramian, M. Eyraud, F. Vacandio, P. Knauth, Cu/Ni/Au multilayers by electrochemistry: a crucial system in electronics – a critical review, Microelectron. Eng. 206 (2019) 25–44, https://doi.org/10.1016/j.mee.2018.12.008.
[2] A. Lennon, J. Colwell, K.P. Rodbell, Challenges facing copper-plated metallization for silicon photovoltaics: insights from integrated circuit technology development, Prog. Photovolt. Res. Appl. 27 (2019) 67–97, https://doi.org/10.1002/pip.3062.
[3] J. Liang, H. Bi, D. Wan, F. Huang, Novel Cu nanowires/graphene as the back contact for CdTe solar cells, Adv. Funct. Mater. 22 (2012) 1267–1271, https://doi.org/10.1002/adfm.201102809.
[4] A. Kraft, C. Wolf, J. Bartsch, M. Glatthaar, S. Glunz, Long term stability of copper front side contacts for crystalline silicon solar cells, Sol. Energy Mater. Sol. Cells 136 (2015) 25–31, https://doi.org/10.1016/j.solmat.2014.12.024.
[5] J. Li, J. Yu, T. Chen, H. Zhang, Q. Wang, P. Wang, Y. Huang, In-situ formation of indium seed layer for copper metallization of silicon heterojunction solar cells, Sol. Energy Mater. Sol. Cells (2020), 110243, https://doi.org/10.1016/j.solmat.2019.110243.
[6] M. Mebarki, A. Layadi, Investigation of the physical properties of Fe/Si for use in a Cu/Fe/Si solar cells contact, Mater. Res. Express (2019), 115505, https://doi.org/10.1088/2053-1591/ab461b.
[7] J. Colwell, P. Hsiao, X. Shen, W. Zhang, X. Wang, S. Lim, A. Lennon, Impact of contact integrity during thermal stress testing on degradation analysis of copper-plated silicon solar cells, Sol. Energy Mater. Sol. Cells 174 (2018) 225–232, https://doi.org/10.1016/j.solmat.2017.09.005.
[8] B. Phua, X. Shen, P. Hsiao, C. Kong, A. Stokes, A. Lennon, Degradation of plated silicon solar module due to copper diffusion: the role of capping layer formation and contact adhesion, Sol. Energy Mater. Sol. Cells (2020), 110638, https://doi.org/10.1016/j.solmat.2020.110638.
[9] L. De Los Santos Valladares, D. Hurtado Salinas, A. Bustamante Dominguez, D. Acosta Najarro, S.I. Khondaker, T. Mitrelias, C.H.W. Barnes, J. Albino Aguiar, Y. Majima, Crystallization and electrical resistance of Cu_2O and CuO obtained by thermal oxidation of Cu thin films on SiO_2/Si substrates, Thin Solid Films 520 (2012) 6368–6374, https://doi.org/10.1016/j.tsf.2012.06.043.
[10] J. Li, J.W. Mayer, E.G. Colgan, Oxidation and protection in copper and copper alloy thin films, J. Appl. Phys. 70 (1991) 2820–2827, https://doi.org/10.1063/1.349344.
[11] M. Twardowski, R.G. Nuzzo, Chemically mediated grain growth in nanotextured Au, Au/Cu thin films: Novel substrates for the formation of self-assembled monolayers, Langmuir 18 (2002) 5529–5538, https://doi.org/10.1021/la020138q.
[12] O.K. Kwon, S.H. Kwon, H.S. Park, S.W. Kang, PEALD of a ruthenium adhesion layer for copper interconnects, J. Electrochem. Soc. 151 (2004) 753–756, https://doi.org/10.1149/1.1809576.
[13] M.J. Cordill, A. Taylor, J. Schalko, G. Dehm, Fracture and delamination of chromium thin films on polymer substrates, Metall. Mater. Trans. A 41 (2010) 870–875, https://doi.org/10.1007/s11661-009-9988-9.
[14] H. Ma, Y. Zou, A.S. Sologubenko, R. Spolenak, Copper thin films by ion beam assisted deposition: strong texture, superior thermal stability and enhanced hardness, Acta Mater. 98 (2015) 17–28, https://doi.org/10.1016/j.actamat.2015.07.013.
[15] I.O. Kruhlov, L.M. Kapitanchuk, S.I. Sidorenko, Z. Erdélyi, T. Ishikawa, S.M. Voloshko, Effect of barrier underlayer on diffusion and phase composition of Ni/Cu thin films under annealing, In: Proceedings of the IEEE 40th International Conference on Electronics and Nanotechnology. 2020. pp. 148–151. https://doi.org/10.1109/ELNANO50318.2020.9088920.
[16] P. Pokorný, J. Musil, P. Fitl, M. Novotný, J. Lančok, J. Bulíř, Contamination of magnetron sputtered metallic films by oxygen from residual atmosphere in deposition chamber, Plasma Process. Polym. 12 (2015) 416–421, https://doi.org/10.1002/ppap.201400172.
[17] A. Lazauskas, V. Grigaliūnas, A. Guobienė, M. Andrulevičius, J. Baltrusaitis, Atomic force microscopy and X-ray photoelectron spectroscopy evaluation of adhesion and nanostructure of thin Cr films, Thin Solid Films 520 (2012) 6328–6333, https://doi.org/10.1016/j.tsf.2012.05.065.
[18] I. Platzman, R. Brener, H. Haick, R. Tannenbaum, Oxidation of polycrystalline copper thin films at ambient conditions, J. Phys. Chem. C 112 (2008) 1101–1108, https://doi.org/10.1021/jp076981k.
[19] I.O. Kruhlov, I.A. Vladymyrskyi, O. Dubikovskyi, S.I. Sidorenko, T. Ebisu, K. Kato, O. Sakata, T. Ishikawa, Y. Iguchi, G.A. Langer, Z. Erdélyi, S.M. Voloshko, Oxidation and reduction processes in Ni/Cu/Cr/Si (100) thin films under low-energy ion irradiation, Mater. Res. Express 6 (2020), 126431, https://doi.org/10.1088/2053-1591/ab6382.
[20] A.K. Orlov, I.O. Kruhlov, A. Lozova, S.I. Sidorenko, S.V. Prikhodko, S.M. Voloshko, The effect of Ar annealing on diffusion and thermal stability of transition metal thin-film systems, Metallofiz. Noveishie Tekhnol. 44 (6) (2022) 735–749, https://doi.org/10.15407/mfint.44.06.0735.
[21] L. Vegard, Die Konstitution der Mischkristalle und die Raumfüllung der Atome, Z. für Phys. 5 (1921) 17–26, https://doi.org/10.1007/BF01349680.
[22] B.C. Johnson, C.L. Bauer, A.G. Jordan, Mechanisms of interdiffusion in copper/nickel thin-film couples, J. Appl. Phys. 59 (1986) 1147–1155, https://doi.org/10.1063/1.336552.
[23] V. Cherepin. Secondary Ion Mass Spectroscopy of Solid Surfaces, first ed., CRC Press, London, 1987 https://doi.org/10.1201/9780429070327.
[24] N. Comini, T. Huthwelker, J.T. Diulus, J. Osterwalder, Z. Novotny, Factors influencing surface carbon contamination in ambient-pressure x-ray photoelectron spectroscopy experiments, J. Vac. Sci. Technol., A 39 (2021), 043203, https://doi.org/10.1116/6.0001013.
[25] V.N. Lipatnikov, A.I. Gusev, P. Ettmayer, W. Lengauer, Phase transformations in non-stoichiometric vanadium carbide, J. Phys.: Condens. Matter 11 (1999) 163–184, https://doi.org/10.1088/0953-8984/11/1/014.
[26] A. Benninghoven, Development in secondary ion mass spectroscopy and applications to surface studies, Surf. Sci. 53 (1975) 596–625, https://doi.org/10.1016/0039-6028(75)90158-2.
[27] P. Hautojärvi, J. Johansson, A. Vehanen, J. Yli-Kaupplia, P. Moser, Vacancy-carbon interaction in iron, Phys. Rev. Lett. 44 (1980) 1326–1329, https://doi.org/10.1103/PhysRevLett.44.1326.
[28] H.B. Zhou, S. Jin, Towards understanding the carbon trapping mechanism in copper by investigating the carbon – vacancy interaction, Chin. Phys. B. 22 (2013), 076104, https://doi.org/10.1088/1674-1056/22/7/076104.
[29] C. Köstler, F. Faupel, T. Hehenkamp, Carbon-vacancy binding in Ni-C alloys, Scr. Metall. 20 (1986) 1755–1759, https://doi.org/10.1016/0036-9748(86)90283-8.